Research article

Hong Mao[a,*], Robin Diekmann[a], Hai Po H. Liang, Victoria C. Cogger, David G. Le Couteur, Glen P. Lockwood, Nicholas J. Hunt, Mark Schüttpelz, Thomas R. Huser, Vivien M. Chen and Peter A.G. McCourt

Cost-efficient nanoscopy reveals nanoscale architecture of liver cells and platelets

https://doi.org/10.1515/nanoph-2019-0066
Received February 28, 2019; revised June 10, 2019; accepted June 11, 2019

Abstract: Single-molecule localization microscopy (SMLM) provides a powerful toolkit to specifically resolve intracellular structures on the nanometer scale, even approaching resolution classically reserved for electron microscopy (EM). Although instruments for SMLM are technically simple to implement, researchers tend to stick to commercial microscopes for SMLM implementations. Here we report the construction and use of a "custom-built" multi-color channel SMLM system to study liver sinusoidal endothelial cells (LSECs) and platelets, which costs significantly less than a commercial system. This microscope allows the introduction of highly affordable and low-maintenance SMLM hardware and methods to laboratories that, for example, lack access to core facilities housing high-end commercial microscopes for SMLM and EM. Using our custom-built microscope and freely available software from image acquisition to analysis, we image LSECs and platelets with lateral resolution down to about 50 nm. Furthermore, we use this microscope to examine the effect of drugs and toxins on cellular morphology.

Keywords: liver; endothelium; optical nanoscopy; fenestration; platelet.

[a]**Hong Mao and Robin Diekmann:** These authors contributed equally to this work.
***Corresponding author: Hong Mao,** Faculty of Health Sciences, Department of Medical Biology, University of Tromsø-The Arctic University of Norway, Hansine Hansens veg 18, Tromsø 9037, Norway, e-mail: hong.mao@uit.no, marcomao1018@gmail.com. https://orcid.org/0000-0003-4266-3550
Robin Diekmann: EMBL Heidelberg, Cell Biology and Biophysics Unit, 69117 Heidelberg, Germany. https://orcid.org/0000-0002-5290-9123
Hai Po H. Liang: ANZAC Research Institute, Concord Repatriation General Hospital, Concord, NSW, Australia
Victoria C. Cogger, David G. Le Couteur, Glen P. Lockwood and Nicholas J. Hunt: ANZAC Research Institute, Concord Repatriation General Hospital, Concord, NSW, Australia; and The University of Sydney, Charles Perkins Centre, Nutritional Ecology and Physiology Lab, Sydney, NSW, Australia
Mark Schüttpelz: Department of Physics, Bielefeld University, 33615 Bielefeld, Germany
Thomas R. Huser: Department of Physics, Bielefeld University, 33615 Bielefeld, Germany; and Department of Internal Medicine and NSF Center for Biophotonics, University of California, Davis, Sacramento, CA 95817, USA
Vivien M. Chen: ANZAC Research Institute, Concord Repatriation General Hospital, Concord, NSW, Australia; and Department of Haematology, University of Sydney, Concord, NSW, Australia
Peter A.G. McCourt: Department of Medical Biology, University of Tromsø-The Arctic University of Norway, 9037 Tromsø, Norway

1 Introduction

The diffraction limit of visible light (~200 nm for blue wavelengths) prevents our use of conventional light microscopy to study a number of biological structures, such as fenestrations (cellular pores ≤200 nm that allow free passage of molecules through cells), mitochondrial ultrastructure, super-fine filopodia, the clustering of filamentous proteins, membrane channels, and many other structures. Previously, such structures were only visible through the use of electron microscopy (EM) on fixed and dehydrated samples, resulting in conclusions where their relevance to hydrated or possibly even living cells is often questionable. Such ultrastructures are of particular biological relevance for the liver and general physiology.

In the human liver, fenestrated liver sinusoidal endothelial cells (LSECs) are an abundant cell type with a total surface area matching that of a tennis court. The fenestrations, which are arranged in groups within "sieve plates," act as plasma filters allowing the passage of nanoparticles, such as lipoproteins, as well as biomolecules and drugs from the plasma for processing by the surrounding hepatocytes [1, 2]. Products secreted by hepatocytes, such as albumin, need to pass through LSECs in the reverse direction to be released to the plasma. As we age, our

LSEC fenestrations become smaller and fewer during age-related defenestration/pseudo capillarization [3]. In addition, a number of compounds/toxins increase/decrease fenestration size or ablate them completely [4, 5]. LSECs also interact with circulating cells such as T-lymphocytes [6] and leukocytes [7], and LSEC fenestrations allow interactions between the villi of circulating T-lymphocytes and the underlying hepatocytes [6]. Platelets, on the other hand, have been proposed to improve liver fibrosis and accelerate liver regeneration [8, 9] via interactions with liver sinusoidal cells.

Platelet interactions with hepatocyte Ashwell-Morell receptors have been proposed as regulating hepatic thrombopoietin production [10]. For this to occur, these platelets would necessarily need to interact first with LSECs to reach the underlying hepatocytes. Indeed, Li et al. [11] proposed a model whereby platelets in liver sinusoids interact with hepatocyte microvilli penetrating LSEC fenestrations. The same authors proposed that Kupffer cells (liver sinusoidal resident macrophages) clear desialylated platelets bound to LSECs in this manner.

Multiple agents can affect LSECs and their fenestrations, for example, in sizes or numbers. Nicotinamide mononucleotide (NMN) is a metabolite crucial for the regulation of nicotinamide adenine dinucleotide (NAD^+) biosynthesis through the NAD^+ salvage pathway [12, 13]. Sildenafil is a medication used to remedy erectile dysfunction and pulmonary arterial hypertension [14]. A previous LSEC study showed increased frequency of fenestrations with NMN and sildenafil treatment, as well as an increased proportion of small fenestrations, suggesting the formation of new fenestrations [15].

Typically, fenestrations and microvilli are studied using methods such as transmission and scanning EM [16–18]. These methods are very powerful but require large and expensive equipment, and considerable technical expertise. In addition, while the morphological information from EM methods is exquisite, it is often challenging to identify proteins within the revealed structures using methods such as immune-EM. Therefore, to study primary LSECs and platelets below the optical diffraction limit, we have developed a low-cost and small, custom-built single-molecule localization microscopy (SMLM) [19–21] instrument capable of visualizing cellular structures simultaneously in two colors and down to about 50 nm resolution.

Multiple groups have developed approaches for cost-efficient super-resolution optical microscopy. Studies have either focused mainly on cost reduction associated with SMLM equipment [22–24], for example, by characterizing highly affordable cameras [25, 26], by using the complementary super-resolution modality super-resolution optical fluctuation imaging [27], or by focusing on single particle tracking [28]. These developments have even included multi-color imaging using sophisticated temporal multiplexing techniques [24] or spectral unmixing [25]. Specific biological applications have mainly been limited to proof-of-concept studies, typically resolving the cytoskeleton or mitochondrial ultrastructure of cultured cells lines. In contrast, we present a cost-efficient setup for SMLM using two low-cost cameras that enable traditional dual-color imaging of spectrally distinct channels at 488 and 647 nm excitation. These channels allow the use of established protocols for sample preparation and a wide selection of fluorescent labels. We apply low-cost SMLM, in the form of direct stochastical optical reconstruction microscopy (dSTORM), to resolve the ultrastructure and the structural response of primary cells to specific treatments. The microscope achieves a good compromise of low cost and small size together with high mechanical stability, low maintenance, and reliable, long-term operation. We show the versatility of this setup by imaging the primary cell types LSECs and platelets with SMLM and the effects of agents/activation on their morphology. This SMLM setup is thus a tool for the cost-efficient super-resolution study of two cell types with a vital role in liver physiology and regeneration.

2 Materials and methods

2.1 Mouse and rat LSEC production

Sprague Dawley male rats and C57/B16 male mice (Animal Resource Centre, Murdoch, Western Australia) were kept under standard conditions and fed standard chow *ad libitum* (Glen Forrest, Western Australia). The experimental protocols were approved by the ethics committee of the Sydney Local Health District Animal Welfare Committee (Approval 2017/012A). All experiments were performed in accordance with relevant approved guidelines and regulations.

2.2 Cell culture protocols, fixation

Male rats (body weight 300–400 g) and mice (~20 g) were anesthetized with a mixture of 10 mg/kg xylazine (Bayer Health Care, CA, USA) and 100 mg/kg ketamine (Ketalar, Pfizer, New York, NY, USA) in saline, and LSECs were isolated and purified as described [29] and plated in serum-free RPMI-1640 (Sigma-Aldrich, Sydney, AU) at 0.2×10^6

cells/cm^2 on fibronectin-coated (Sigma-Aldrich, Sydney, AU) 16-well chambered #1.5 coverslips (Grace Bio-Labs CultureWell™ removable chambered coverglass, Sigma-Aldrich, Sydney, AU) for 3 h in RPMI-1640. LSECs were then fixed with 4% paraformaldehyde (ProSciTech. Pty Ltd, Thuringowa, AU) in phosphate buffered saline (PBS) and 0.02 M sucrose (Sigma-Aldrich, Sydney, AU), pH 7.2, for 15 min, and stored under PBS. After fixation, the cells were prepared for visualization prior to applying on dSTORM [30].

2.3 Platelet preparation

Blood from healthy human donors (ethical approval: Concord RG Hospital Ethics Board no. HREC/15/CRGH/54) was collected from antecubital fossa via a 21G butterfly needle into 3.2% citrate-containing tubes (Becton Dickinson, Sydney, AU). Washed platelets were prepared from citrated blood as described [31]. Briefly, platelet-rich plasma was isolated by brake-free centrifugation for 10 min at 200×*g* and mixed gently by inversion in a 1:1 ratio with Tyrode's buffer (137 mM NaCl, 2.5 mM KCl, 0.5 mM $MgCl_2$, 12 mM $NaHCO_3$, 0.36 mM Na_2HPO_4, 10 mM HEPES, 5.5 mM glucose, and 0.25% human serum albumin, pH 7.5) containing 1 μM prostaglandin E1 (PGE_1), (Sigma-Aldrich, Sydney, AU). Platelets were then pelleted by brake-free centrifugation for 15 min at 650×*g*, washed once with Tyrode's buffer, and pelleted again, before resuspension in Tyrode's buffer to 1×10^6 platelets per 100 μl. The platelets were allowed to rest for 20 min before further manipulation. The platelets were then plated in removable chambered coverglass wells (see above) in Tyrode's buffer. After platelet wash, 2 U/ml of thrombin (Sigma-Aldrich, Sydney, AU) was added for 10 min at room temperature (RT) to stimulate the platelets, followed by fixation as above.

2.4 Cell staining

All fixed samples were washed with PBS. For membrane staining, cells were stained with Vybrant DiD (1:200, ThermoFisher) for 20 min, or Cell Mask Green (1:1000, ThermoFisher) for 10 min at RT, or BODIPY FL C5-Ganglioside GM1(1:200, ThermoFisher) for 15 min at RT.

For cytoskeleton staining, cells were permeabilized for 90 s with 0.5% Triton-X100 and washed two to three times with PBS. Non-specific binding was blocked with 5% bovin serum albumin in PBS for 45 min at RT. Cells were incubated with the primary antibody (1:500, monoclonal anti-α-tubulin, Sigma-Aldrich, Sydney, AU) for 1 h at RT, and then washed three times for 10 min with 0.1% PBS Tween-20. The secondary antibody (1:1000, Anti-mouse IgG, AlexaFluor 647 or 488 conjugate, CellSignaling, Arundel, AU) was applied for 1 h at RT. The staining solution was removed and the cells were then washed with 0.1% PBS Tween-20 (Sigma-Aldrich, Sydney, AU) (three times for 10 min) then PBS. Phalloidin AlexaFluor 488 (AF488) or AlexaFluor 647 (AF647) (1:40, ThermoFisher, Sydney, AU) was applied for 20 min at RT. Cells were washed with PBS.

All samples were mounted in imaging buffer (see imaging conditions and composition of buffers in Supplementary Tables 1 and 2, respectively). We used either OxEA [Oxyrase-based oxygen depletion supplemented with β-mercaptoethylamine (MEA), Sigma-Aldrich, Sydney, AU] buffer [32] [3% (v/v) Oxyfluor, Oxyrase Inc. Mansfield, 40.5 units/ml], GODCAT-1 (glucose oxidase and catalase-based oxygen depletion and hydrogen peroxide depletion) buffer [33] [50 μg/ml glucose oxidase (Sigma-Aldrich, Sydney, AU), 1 μg/ml (50 units) catalase (Sigma-Aldrich, Sydney, AU), 40 mg/ml glucose (Sigma-Aldrich, Sydney, AU), 1.25 mM KCl and 1 mM Tris] including 100 mM MEA, 2.5% glycerol (Sigma-Aldrich, Sydney, AU) and 200 μM Tris (2-carboxyelthyl) phosphine hydrochloride (Sigma-Aldrich, Sydney, AU), or GODCAT-2 buffer (50 mM MEA, 0.5 mg/ml glucose oxidase, 40 mg/ml catalase). After the buffer was applied in the cell chamber, excess buffer was removed by sliding a coverslip onto the chamber to prevent oxygen permeation.

2.5 Imaging

Rat (Figures 1D, 3, 4) and mouse (Figures 1C, 5) LSECs were imaged on the custom-built dSTORM setup described below, using 488 and 647 nm lasers (Coherent, Santa Clara, CA, USA) and two CMOS cameras (IDS-Imaging Development Systems, Obersulm, DE). A 60×/NA = 1.49 oil immersion total internal reflection fluorescence (TIRF) objective lens (Olympus, Center Valley, PA, US) or a 60×/NA = 1.4 oil immersion objective lens (Olympus, Center Valley, PA, US) was used. For dual-color images, first the deep red channel (647 nm excitation) was imaged, followed by the green (488 nm excitation) channel. In general, 20,000 to 45,000 frames were collected at 50 to 100 fps with image sizes of 344×344 or 400×400 pixels for rat LSECs, and 144×144 or 200×200 pixels for platelets. CMOS cameras were controlled via Micro Manager [34], using a modified device adapter [26]. The lasers were controlled using the manufacturer's software.

2.6 Optical setup

Our custom-built wide-field dSTORM microscope uses two solid-state lasers of 488 and 647 nm wavelengths (Figure 1). The latter is fiber-coupled to allow for easy handling. After adjusting the beam diameters using a collimation lens and/or telescopes, the beams are overlaid via a dichroic mirror and focused onto the back focal plane of the objective lens for sample illumination. Mounting the relevant parts of the illumination unit on a translatable stage allows for easy switching between epi-fluorescence (epi), highly inclined and laminated optical sheet (HILO) [35], and TIRF [36] configuration. The system has sufficient degrees of freedom such that both lasers can be optimally aligned to illuminate a sample mounted on an xy-stage. Focusing is performed manually by a precise z-translation stage holding objective lens. The fluorescence emission is separated from excitation by a dichroic mirror and the emission is further separated by emission wavelength using a second dichroic mirror. A detailed part list together with assembly and alignment instructions is supplied in the Supplementary material.

We placed a separate tube lens into every detection path behind the dichroic excitation beam splitter. In doing so, the collimated, but not focused, part of the

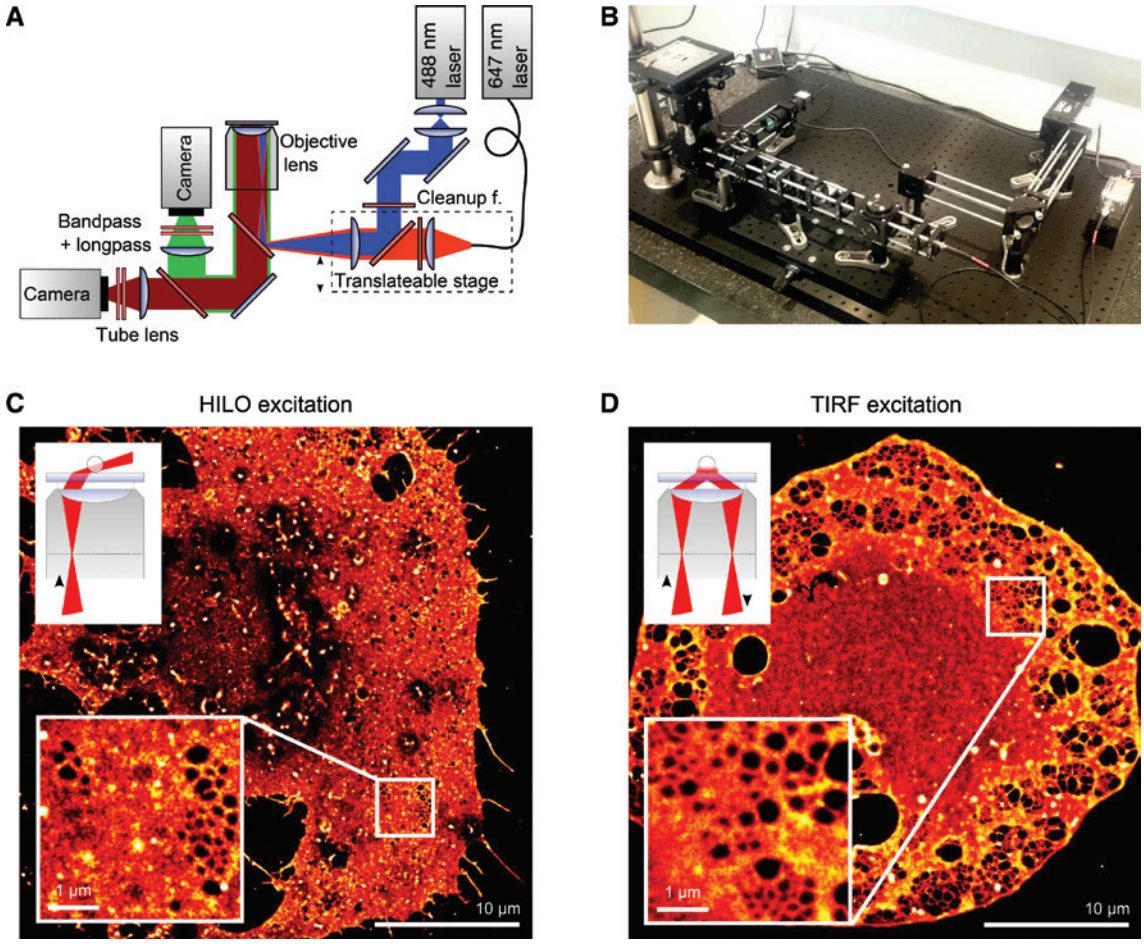

Figure 1: The cost-efficient dual-color dSTORM microscope.
Schematic (A) and photograph (B) of the microscope showing the free standing 488 nm and fiber pig-tailed 647 nm laser that are combined by a dichroic mirror. The lasers are focused to the back focal plane of the high NA objective lens, while a translatable stage allows for shifting the focus in the back focal plane and therefore to conveniently switch between epi, HILO (C), and TIRF (D) illumination. The fluorescence collected by the objective lens is separated from the excitation and spectrally split onto two CMOS cameras. (B) Mounting the optical components into a cage system results in high mechanical stability. Open space on the black breadboard shows that the 0.5 m^2 used could in principle have been reduced by a factor of about 2. However, this layout was chosen to provide the option of including further lasers of different wavelengths. dSTORM images of both (C) Vybrant DiD stained mouse LSECs using HILO illumination (inset) and (D) Vybrant DiD stained rat LSECs using TIRF illumination visualize sub-diffraction limit sized membrane fenestrations at high image quality. Insets in (C) and (D) show fenestrations within sieve plates in more detail.

beam is transmitted through the dichroic beam splitter. In contrast, using a single tube lens for both channels would require its placement before the dichroic beam splitter. Arimoto and Murray showed that a tilted glass plate can cause serious aberrations when transmitting a focused beam in a medium of a different refractive index [37]. This effect is avoided in our setup, where the dichroic beam splitter results in a minor lateral displacement of the beam, but does not lead to serious optical distortions.

Raw data were acquired using a dedicated industry-grade CMOS camera in each color channel. Multiple industry-grade CMOS cameras that feature sufficiently low noise and high sensitivity are available [22, 25]. We chose a camera model using the Sony IMX174 sensor (UI-3060CP Rev.2; IDS-Imaging Development Systems, Obersulm, DE), which we previously characterized extensively and found to perform close to a commonly applied scientific-grade camera, but at a fraction of the cost [26]. The quantum efficiency of the sensor is about 77% at 520 nm and about 45% at 676 nm [26]. The detector characterization was performed using multiple thousands of frames recorded at different light levels as described by Huang et al. [38] and Diekmann et al. [26]. Data for the cameras used in this study can be found in the Supplementary information of Diekmann et al. [26] (Supplementary Figures 2–4, CMOS 2 and CMOS 3). To provide an impression of the quality of the raw data we collected, we provide 500 frames each for the images shown in Figures 3A, E, 5H and 6A as Supplementary data.

2.7 Image reconstruction

The freely available software package Fiji [39] was used for image processing and analysis, including dSTORM reconstruction [40], registration of multi-color images (bUnwarpJ plugin [41]), super-resolution image analysis (SQUIRREL plugin [42]) particle size measurement, line profile measurements, application of look-up tables, cropping, and image export.

The projected pixel size was determined by a calibration sample and deviated less than 2% from the theoretical value of 109.9 nm. After finding the single-molecule positions with sub-pixel accuracy using the single emitter fitter of ThunderSTORM, post-processing with drift correction (ThunderSTORM, using the image cross-correlation algorithm, number of bins = 3–7; magnification = 5) was applied if necessary. Localization merging within subsequent frames and spatial proximity as well as filters based on the localization table was applied subsequently, if necessary. Other super-resolved images were reconstructed using the free software rapidSTORM [43] (Figure 4A–F and H, I, K, L). In rapidSTORM, we used the same pixel size as ThunderSTORM. rapidSTORM is stand-alone software requiring the user to specify the workflow of the fitting and reconstruction algorithm by choosing certain modules. To do so, the "Count localizations," "Display progress," and "Cache localization" modules were added under the "dSTORM engine output" module to process the data and the "Expression filter" output module was added under the "Cache localization" module to allow for filtering based on the individual localization properties such as photon count. Furthermore, the "Localizations file" and "Image display" modules were displayed under the "Expression filter" module to have the data stored and the image displayed accordingly.

2.8 Fenestration and actin quantification

Fenestration detection and actin stress fiber detection were performed using the pixel classification workflow in the freely available machine learning image processing software Ilastik [44]. For the fenestration size analysis, the two classes of fenestrations and membranes were manually annotated and iteratively refined in a few locations for every cell, but the same classification was used for all cells. The automatically segmented fenestrations were then exported to Fiji [39]. The size was determined using Fiji's "Analyze Particles" plugin with a circularity of 0.6–1.0. The resulting table was imported into MATLAB (Mathworks); the area was translated to the diameter of a corresponding circle of the same area and filtered for diameters ranging from 54 to 401 nm prior to binning. For the actin stress fiber analysis, the three classes of actin stress fibers, other actin fibers, and background were manually annotated and iteratively refined in a few locations for every cell, but the same classification was used for all cells. The segmentation was exported to Fiji and the area covered by the stress fibers and the entire actin network was determined from the segmentation.

3 Results

3.1 Schematic of the low-cost microscope for SMLM

Our custom-built microscope is shown in Figure 1A and B. A full list of all components, their suppliers/

catalogue numbers, cost, and detailed assembly instructions is provided in the Supplementary material. Fluorescence is excited with 488 and 647 nm lasers and the emission is split into two cameras for conventional dual-color imaging. The optical breadboard (Figure 1B) has sufficient "free real estate" to house more lasers and cameras if desired, and the dichroic filter used allows for the additional inclusion of, for example, 405 and 532 nm lasers.

3.2 Cost-saving features

We evaluated the use of available objective lenses from our obsolete microscope park to reduce costs even further. We anticipate that many biomedical laboratories face a similar situation, where spare, high-quality objective lenses (e.g. from obsolete confocal microscopes) are available. Directing the lasers via a translatable stage into our microscope (Figure 1A) allows the use of standard (i.e. non-TIRF) objectives for epi and HILO illumination. Using an oil-immersion $60\times/\mathrm{NA}=1.40$ objective lens from an obsolete Olympus microscope, individual fenestrations of mouse LSECs were resolvable with dSTORM [30] (Figure 1C, inset). Due to diffraction-limited resolution, fenestrations sized below 200 nm cannot be visualized in conventional wide-field imaging with the same objective. For comparison, a TIRF lens on the same microscope can similarly be used to resolve individual fenestrations of rat LSECs (Figure 1D). Given that the $60\times$ TIRF objective we acquired specifically for this microscope costs €6350, using spare objectives instead would represent significant savings.

In many cases, SMLM microscopes are set up on vibration dampened optical tables. If these microscopes are not mechanically isolated, oscillations from the environment (e.g. air conditioning units, etc.) can easily exceed the spatial resolution this microscopy can achieve and thus attenuate the quality of the super-resolution images. To mechanically isolate our microscope, without the cost of a dampened optical table, we set the microscope up on an aluminum breadboard placed on an inflated bicycle inner tube at a relative pressure of 0.5 bar (Figure 2A). Inclusion of this inner tube significantly reduced vibrations, as shown by the repeated localization of the center of bright, fluorescent beads of 100 nm diameter (Tetraspeck; ThermoFisher) (Figure 2B). The achieved full-width-at-half-maximum (FWHM) values for the localization cloud from one bead of 7.9 nm correspond to an effective precision of about 3.3 nm. This precision is much better than what we achieved localizing single molecules in dSTORM experiments (Figure 3); hence potential remaining vibrations are not a major resolution-limiting factor.

For further savings, we chose not to build the microscope around a costly conventional microscope body, but set up the microscope using almost exclusively off-the-shelf optics and optomechanical components. This provided us the flexibility to plan and build it such that high mechanical stability with very low lateral drift of less than 50 nm over more than 1 h was achieved (Figure 2C). Additional axial drift can lead to the loss of the focus over time. We tested multiple options for high mechanical stability without the need for costly active components (such as piezo actuators and position sensors) and found a z-translator that achieved almost perfect focal stability. Our 2D imaging experiments do not allow us to access the z-position directly, but the high focal stability is indicated by the median value of the point spread function FWHM remaining almost constant over more than 1 h (Figure 2D). Although lateral drift in particular could not be prevented entirely in all experiments, a conventional drift correction routine was able to correct for the residual drift and restore fine image details such as fenestrations in LSECs (Supplementary Figure 2C and D). Other image reconstructions did not require drift correction at all (Figure 3A and B). Noticeably, the image shown in Figure 3A was recorded 11 months after the microscope was originally set up and no further optical realignment had been performed during this time. This is another indicator for the high mechanical stability of the microscope, not only allowing for long-term SMLM image acquisitions but also resulting in low maintenance requirements.

While a UV laser (such as 405 nm) is a preferred choice for active photo-switching of dyes to the fluorescent on-state in SMLM modalities such as dSTORM, we did not include it in our setup to reduce costs and complexity. However, the existing 488 nm laser can also be used for effective photo-switching of organic dye molecules that are excited using the 647 nm laser (Figure 2E). The 488 nm laser can therefore serve the two purposes of (1) exciting dyes in the green spectral region and (2) photo-switching dyes of the far-red spectral region.

For dual-color imaging, the excitation profiles can be optically well aligned to illuminate the same part of the sample (Figure 2F). On the other hand, optical alignment alone of the two emission channels left residual deviations of more than 400 nm locally (Figure 2G), giving rise to the need of post-acquisition registration which, however, is a standard procedure in traditional multicolor imaging.

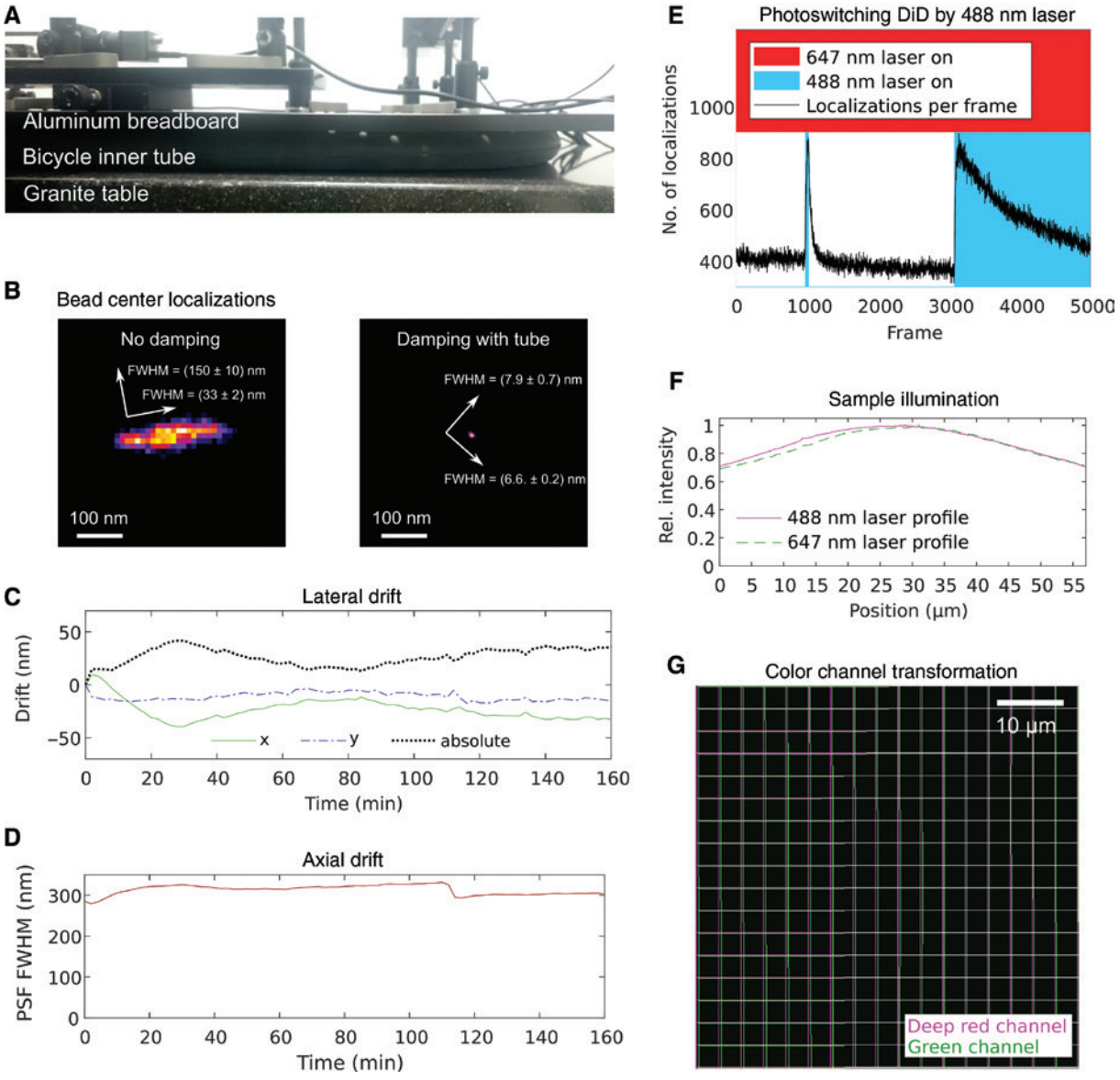

Figure 2: Mechanical and optical characterization of the custom-built dSTORM microscope.
(A) Side view of the microscope setup showing the bicycle inner tube for vibration damping. (B) The vibrations of the microscope are characterized by the repeated, high frame rate localization of the center of a sub-diffraction limit sized fluorescent bead. When damping the vibration with the inner tube in place, the remaining motion blur is well below the resolution of the microscope. (C) Plot of lateral drift as a function of time for repeated localizations of a fluorescent bead shows that the drift is below 50 nm over more than 1 h. (D) The point spread function width does not considerably change during this time, indicating high focus stability. (E) Vybrant DiD localizations as a function of time when using the 647 nm for fluorescence excitation and the 488 nm laser for photo-switching to the on-state in defined time intervals. (F) The different lasers are well overlaid for sample illumination using a beam profile that maintains about 80% of its peak intensity over a disk of 40 µm in diameter. (G) The color channel transformation between the two channels (transforming the green onto the deep red channel) measured by beads simultaneously emitting in both channels.

3.3 Visualizing the nanoscale architecture of LSEC plasma membranes and the actin cytoskeleton

LSEC membranes (and the fenestrations within) as well as the cytoskeleton have previously been visualized by dSTORM super-resolution microscopy using Cell Mask Deep Red, Vybrant DiD, and antibodies or phalloidin conjugated with AlexaFluor 647 (AF647), AlexaFluor 488 (AF488), or Atto488 [45–47]. We tested a variety of buffers and stains on LSECs and platelets (Supplementary Note 1). Phalloidin-AF488 in OxEA buffer resulted in actin images of high quality (Figure 3A–D), while Vybrant DiD in GODCAT buffer resulted in membrane images of high quality (Figure

3E–H). These are indicated by SQUIRREL analyses [42] showing a resolution-scaled Pearson coefficient better than 0.9 (Figure 3C and G). The resolution-scaled error (RSE) particularly increases in regions of higher actin density (Figure 3C) and membrane structures distant from sieve plates, both possibly because of multi-emitter artifacts due to the relatively high emitter density (Figure 3I). However, the low RSE values in regions of sieve plates confirm the ability of analyzing the fenestration size at high confidence [46]. Due to the relatively low quantum efficiency of the industry-grade CMOS cameras in our microscope, observed photon counts per localization (Figure 3J) as well as background signal (Figure 3K) were not as high as in former studies [46] and [45], resulting in average localization precisions of 20 to 24 nm (Figure 3L). The particularly good Fourier ring correlation (FRC) resolution [48] of down to 38 nm (Figure 3H) correlates with regions of bad RSE values (Figure 3G), confirming other researchers' findings that the FRC resolution might be an inferior resolution metric in SMLM [49, 50]. As suggested by Legant et al. [49], we additionally calculated the geometric sum of 2.4 times the mean localization precision (i.e. inferring the best possible resolution from the localization precision) equal to 57.8 nm and the 10 times oversampled Nyquist-limited resolution equal to 10.4 nm that we estimated from the localization sampling of the plasma membrane of 3 million localizations per 81 μm^2 (Figure 3F). The resulting estimated resolution is 58.7 nm. As the resolution can be locally slightly increased, we conclude that we can measure fenestration sizes down to approximately 54 nm in our dSTORM images.

The dense localization sampling of the plasma membrane that allows for this high Nyquist resolution is particularly challenging for the SMLM fitting and reconstruction software. The SMLM community has produced a magnificent amount of different software solutions for SMLM data reconstruction, post-processing, and analysis [51, 52]. While it is beyond the scope of our work to extensively compare and evaluate the broad variety of software packages, we would like to point out the two software packages we used for image reconstruction in this study. ThunderSTORM [40] is a good option for inexperienced users since it comes as an ImageJ/Fiji plugin [39]. The user can therefore navigate in an environment already familiar to many researchers in the field of fluorescence microscopy. While ThunderSTORM also offers experienced users the options to tweak many parameters of the reconstruction pipeline, its default settings often yield respectable results, making it a good choice even for inexperienced users. However, reconstructing images of LSEC membranes is a particularly challenging task due to the high localization density. A lot of single emitter events must first be fitted for one reconstruction of high quality and then also be stored in the memory. Unfortunately, ThunderSTORM runs relatively slowly during the fitting algorithm and demands a lot of memory, easily filling the memory even for a high-end desktop computer. We therefore used rapidSTORM [43] as a complementary

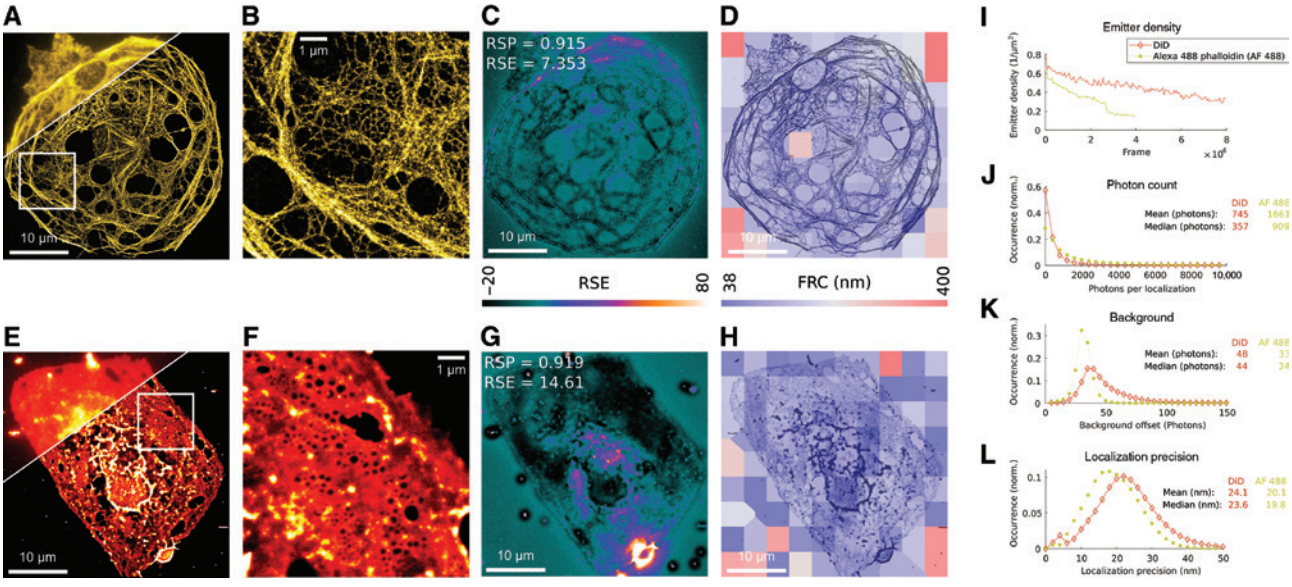

Figure 3: dSTORM imaging quality characterization.
Rat LSEC diffraction limited (A, E, upper left) and dSTORM images of actin (A, B) stained with AF488-phalloidin and membrane (E, F) stained with Vybrant DiD. Spatially dependent dSTORM image quality metrics of RSE (C, G) and FRC resolution (D, H) determined by SQUIRREL. (I) Emitter density in the ROI of (B, F) as a function of the frame. (J–L) The single molecule localization statistics (AF488 and DiD) as photon counts per localization, background and localization precision.

option for SMLM data reconstruction. As suggested by its name, it runs relatively quickly during the reconstruction and furthermore is relatively memory efficient. This made it our preferred choice for reconstruction of the membrane structure. The two different software packages ThunderSTORM and rapidSTORM produced comparable results when reconstructing the same data set of immunostained tubulin recorded with our microscope (Supplementary Figure 1B and C). Both reconstructions show the significant resolution improvement as compared to the diffraction-limited wide-field image that we recorded before acquiring the dSTORM data (Supplementary Figure 1D).

3.4 dSTORM imaging of LSECs challenged with exogenous agents

Recently, a number of agents (NMN and sildenafil among others) were demonstrated to enhance fenestrations size and number in LSECs from aging mice, as visualized with scanning EM [15]. We tested these agents in our optical super-resolution microscope (Figure 4) and visualized changes in the actin cytoskeleton in cells treated with NMN (Figure 4B and E) and sildenafil (Figure 4C and F). Especially on sildenafil treatment, actin stress fibers became clearly pronounced (Figure 4M) as measured in a machine learning assisted workflow (Methods, Supplementary Figure 4). F-actin in the sildenafil-treated cells appears to be generally more condensed, and the actin rings (arrows, Figure 4E and F) that typically delineate fenestrations [47] are more pronounced in both NMN and sildenafil-treated cells. We also noted similar changes in fenestration size (Figure 4H, I, K, L) as reported in [15]. NMN and sildenafil increased the median fenestration diameter by 5% and 30%, respectively (Figure 4N). While the use of EM for the quantitative analysis of fenestration morphology is a well-established tool, the use of dSTORM for the same purpose makes certain steps in the workflow (such as sample preparation) much easier, and, in particular when using a low-cost implementation as presented here, drastically lowers the instrument cost. Furthermore, the use of fluorescence super-resolution microscopy combines high resolution with specificity such that the users can get the best of both worlds, which makes quantitative actin analysis accessible.

3.5 Super-resolution imaging of lipid rafts on LSECs

Svistounov et al. [53] previously demonstrated the presence of lipid rafts on LSECs and proposed that these play a role in the regulation of fenestration size. Using our microscope, we found that Bodipy FL C5-ganglioside GM1 (BodipyGM1), a lipid raft stain, photo-switches in GODCAT-1 buffer. This confirms the work of Bittel et al. [54], who recently reported photo-switching of Bodipy FL for dSTORM. Interestingly, the C5-ganglioside GM1 conjugated form of Bodipy FL not only visualized lipid rafts but also stained all of the LSEC plasma membrane, with some areas of higher localization density probably being indicative of lipid rafts (Figure 5A and B). We achieved a sufficiently low blinking density to allow for high-resolution dSTORM imaging of the LSEC plasma membrane (Figure 5B and C), at a mean photon count of 831 photons per localization (Figure 5D), together with a mean background of 102 photons (Figure 5E), resulting in an average localization precision of about 19 nm (Figure 5F). The mean on-state lifetime was 1.7 frames per fluorophore (Figure 5G) when using single frame exposure times of 20 ms. Interestingly, fenestrations were also visible with BodipyGM1 staining (Figure 5B, H, and I), allowing the simultaneous imaging of fenestrations and structures (lipid rafts) that are proposed to regulate their size [53]. Choosing a look-up table with high contrast throughout a large scale, Figure 5H shows how the low-density BodipyGM1 staining (blue) is distributed over the entire cell and visualizes fenestrations. The high-density of BodipyGM1 staining (green to white) is distributed throughout the cell in discrete points, long sinuous structures, or patches. Figure 5I shows one such patch (arrow) adjacent to a sieve plate (dashed circle), which also contains some discrete punctuated BodipyGM1 staining within. The long sinuous patches have been reported previously on BodipyGM1-stained LSECs using TIRF microscopy [53]. We attempted double staining of LSECs with Vybrant DiD and BodipyGM1 on our setup, but were not successful. However, we achieved this co-staining using structured illumination microscopy (not shown) where we saw some overlap of BodipyGM1 and Vybrant DiD staining. This is to be expected since lipid rafts are membrane structures, but there were areas where BodipyGM1 staining was elevated relative to Vybrant DiD staining, and therefore indicative of elevated lipid raft membrane components.

3.6 Imaging platelets by dSTORM

Given that platelets play an active role in the resolution of hepatic fibrosis and liver regeneration [8, 9], we also investigated the utility of our microscope for the study of these cells. We successfully tested phalloidin-AF647 (actin stain) and Vybrant DiD (membrane stain) (Figure 6, Supplementary Figure 5). Unstimulated discoid platelets

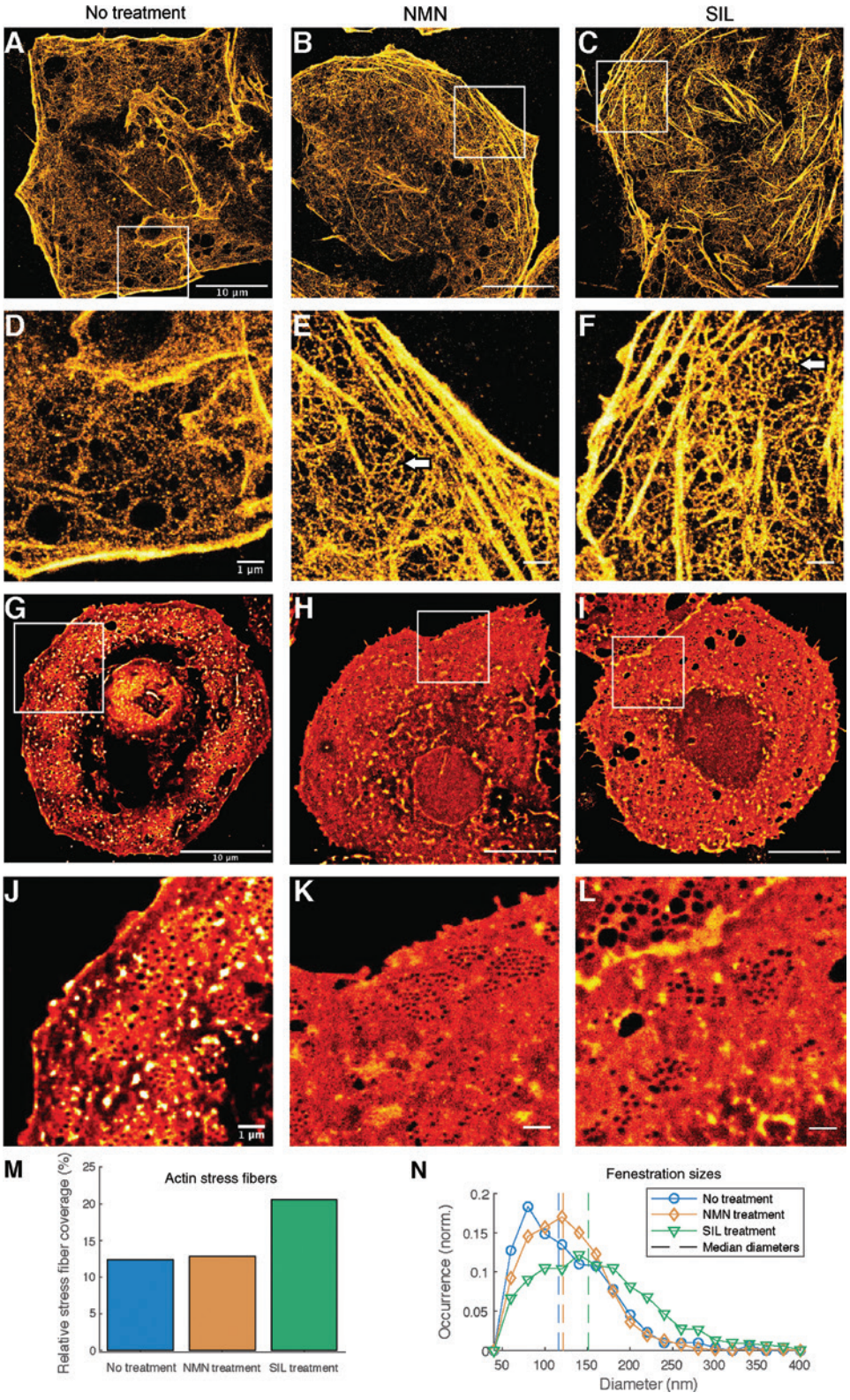

Figure 4: Membrane and actin staining in LSECs treated with NMN and sildenafil.
(A–F) dSTORM images of drug-treated rat LSECs in OxEA buffer, stained for actin with phalloidin-AF488: (A, D) Control; (B, E) 333 µg/ml NMN; (C, F) 60 ng/ml SIL. Insets (D–F) show a detailed comparison of drug effects compared to controls. Arrows in E and F indicate actin rings that typically delineate fenestrations. (G–I) Images of drug-treated rat LSECs, stained with Vybrant DiD in GODCAT-1 buffer, (G, J) Control; (H, K) NMN; (I, L) SIL. (M) Plot of relative percentage of stress fibers as a total of actin staining vs. control, NMN and SIL treatment (n = 1 for each point). The relative proportion of stress fiber actin within total actin increases particularly upon SIL treatment. (N) Histogram of occurrence vs. fenestration size after challenge with NMN and SIL. Fenestration size increases after NMN and SIL treatment. All imaging was in TIRF mode.

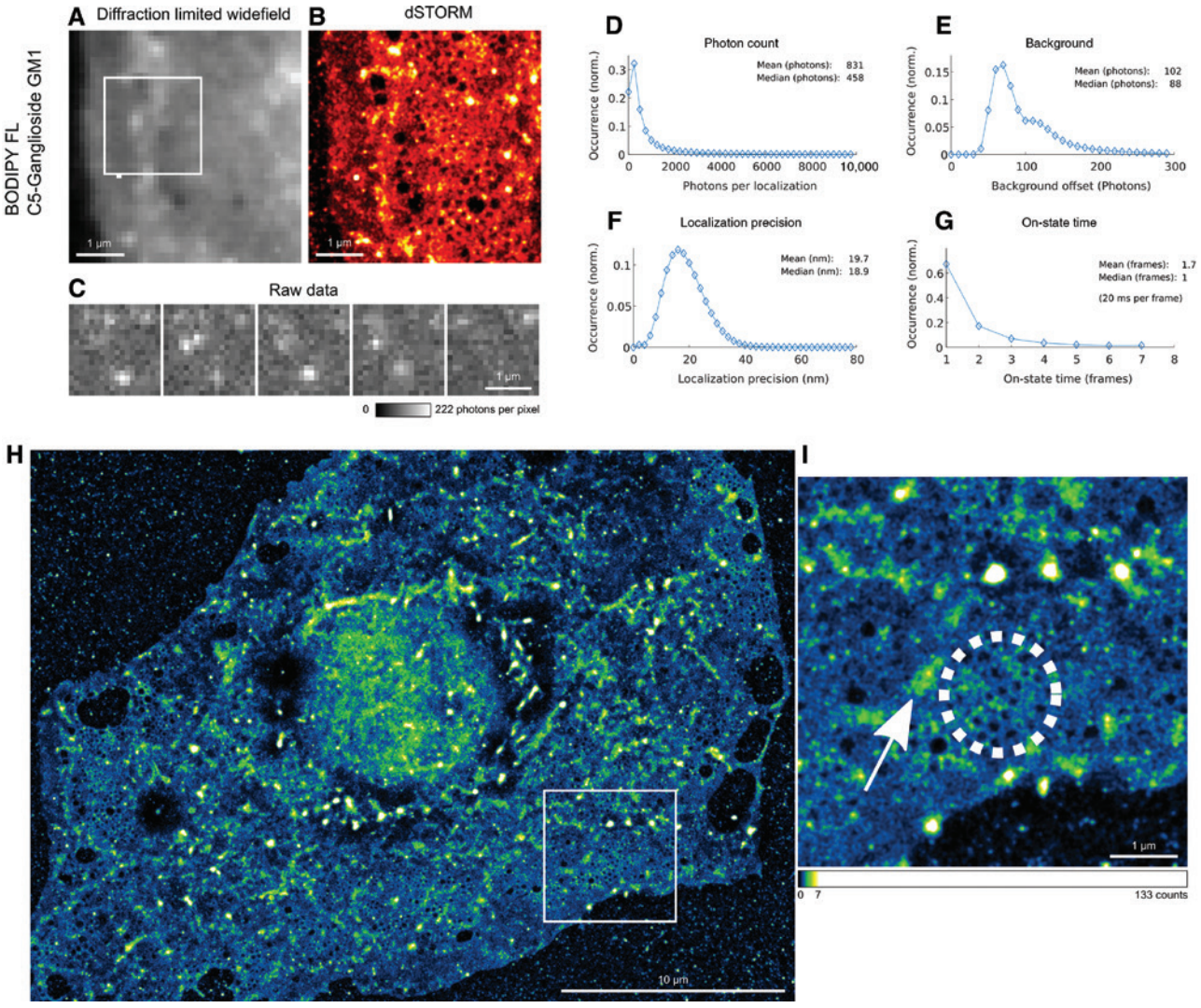

Figure 5: Bodipy FL C5-ganglioside GM1 visualizes lipid rafts and fenestrations.
(A) Diffraction limited and (B) dSTORM images of BodipyGM1-stained mouse LSECs show the resolution enhancement in the dSTORM image, where membrane fenestrations become visible. (C) Representative raw data of photo-switching BodipyGM1 in subsequent frames of the area indicated by the box in (A). (D–G) show the single molecule (Bodipy) localization statistics as photon counts per localization, background, localization precision and on-state-lifetime histograms. (H) An entire LSEC stained with BodipyGM1 processed with a high-contrast look-up table. Blue indicates low-density BodipyGM1 staining, while green to white indicates high-density BodipyGM1 staining. (I) The inset from (H) shows the proximity of a sieve plate (encircled with white dashes) to a putative lipid raft (indicated by a white arrow).

adopt a round shape on contact with imaging surface (Figure 6H–J, Supplementary Figure 5A and B). After thrombin stimulation, platelets begin to spread and actin-rich cell protrusions (filopodia) forming a spindle-like morphology appeared (Figure 6K–M, Supplementary Figure 5C and D). Up to 7 µm long and about 100 nm wide filopodia were often seen emanating from the platelet plasma membrane in thrombin-stimulated platelets (Figure 6M). Filopodia are characterized by organized actin fibers arranged in parallel bundles, while lamellipodia are intermediate areas between individual filopodia in which the actin is orthogonal to the membrane. These structures have previously been reported in EM studies of platelets [55]. Double staining allows the relationship between actin and membrane to be visualized in these structures (Figure 6M).

3.7 Evaluation of double-staining methodologies with our microscope

By screening a combination of dyes allowing for multicolor dSTORM imaging of platelets, we discovered that the membrane stain Cell Mask Green (Figure 6A) photoswitches in GODCAT-1 buffer. To the best of our knowledge, photo-switching of Cell Mask Green has not been

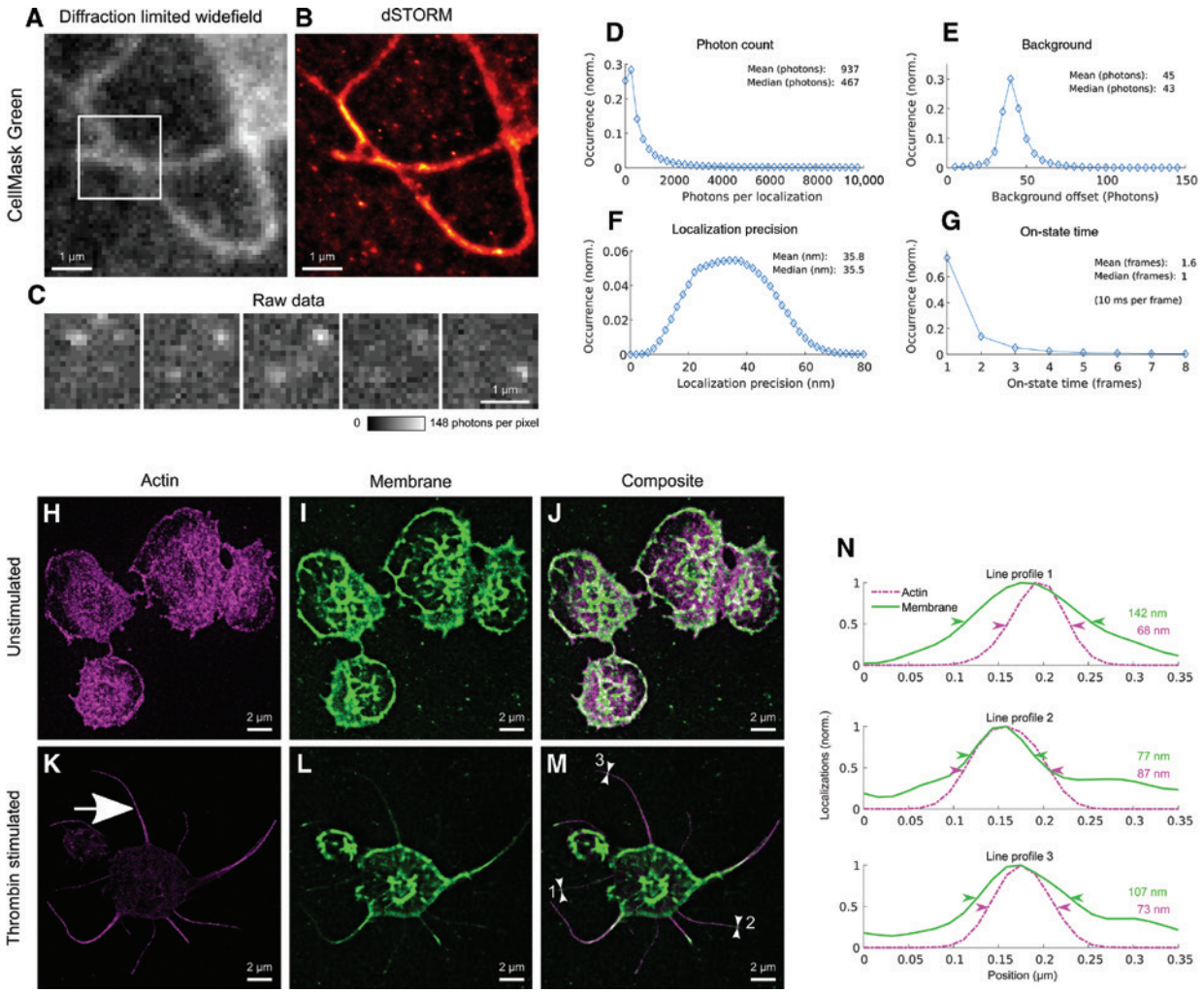

Figure 6: Dual color staining of human platelets.
(A) Diffraction limited and (B) dSTORM images of Cell Mask Green stained thrombin-stimulated platelet plasma membrane extensions. (C) Representative raw data of photo-switching Cell Mask Green in subsequent frames of the area indicated by the box in (A). (D–G) The single molecule localization statistics (Cell Mask Green) as photon counts per localization, background, localization precision and on-state-lifetime histograms. (H–M) Dual-color dSTORM images of human unstimulated (H–J) and thrombin stimulated (K–M) platelets stained with phalloidin AF647 (H, K) (purple) and Cell Mask Green (I, L) (green). (J, M) merged phalloidin AF647 and Cell Mask Green images. (N) The line profile analysis of (M) regions 1, 2, and 3 indicated within the figure shows that the ultra-thin membrane projections contain polymerized actin (white arrow in (K)). The numbers report the FWHM values of the membrane and actin structures, respectively. Imaging was performed in TIRF mode.

reported previously, and this enabled dSTORM imaging of the platelet membrane (Figure 6B). Sparse single-molecule blinking occurred at illumination intensities of 620–2330 W/cm^2 from the 488 nm laser (Figure 6C). Single molecules were detected at a mean photon count of 937 photons per localization (Figure 6D) and a mean background of 45 photons (Figure 6E). The resulting average localization precision was 36 nm (Figure 6F) and the mean on-state lifetime was 1.6 frames per fluorophore when using single frame exposure times of 10 ms (Figure 6G). We used Cell Mask Green to co-stain and simultaneously image actin using phalloidin AF647 in the same buffer (Figure 6H, J, K and M). Using this strategy for dSTORM, we found that the ultra-thin membrane projections (Figure 6M) contained a scaffold of polymerized actin (Figure 6K–N).

4 Discussion

In this work we demonstrate a simple and cost-effective dSTORM microscope using off-the-shelf components. The total cost of the microscope, including the new TIRF objective lens, was about €30,000 (Supplementary material). Using objective lenses from obsolete microscopes, and low-end lasers [23], this can be reduced to about €15,000. However, we chose higher quality lasers to guarantee stability and

low maintenance for microscope users with little experience in handling lasers and other optical components. Furthermore, air tables costing in the range of €7000–15,000 are unnecessary, as using a bicycle inner tube under our breadboard was sufficient to isolate building vibrations.

With our custom-built SMLM microscope, we resolved LSEC fenestrations from mice and rat livers. Mouse and rat LSEC fenestrations are highly similar in morphology and organization, and are similarly difficult structures to visualize, as it is the absence of staining that visualizes a fenestration. In this context, background staining can obscure the structure. Background staining and other sources of noise therefore require extra attention. That said, the industrial CMOS cameras used in this study provided sufficient wide-field fluorescence image data, easily detected single blinking fluorescent molecules, and the read noise of about 6.4 electrons per pixel was not an issue. While the performance of this particular CMOS camera was extensively evaluated in a previous study [26], we note that there are other, even cheaper industry-grade cameras available [22, 25]. Additionally, other microscope components such as optomechanics might in principle be replaced by other manufacturers' solutions or custom-made parts. This opens up the possibility of choosing the ideal hardware for the specific applications of advanced users.

Advanced users can also easily start from our build (which is documented in detail in the Supplementary material) and modify it according to their needs. Many groups have described solutions for cost-effective, small, and accessible microscopes for SMLM [22–25, 28, 56]. We would like to encourage advanced users to gather inspiration from the broad variety of suggested options and decide what suits best for their particular application – just as we did for this work. While other researchers have presented significantly cheaper and/or smaller microscopes for SMLM, our aim was to achieve sufficient image quality particularly for the task of studying the cell types described in this study and using traditional multi-color imaging at high mechanical stability and low maintenance on a particularly easy to use microscope, even for users with little SMLM experience. While achieving these goals, the microscope is significantly cheaper than commercially available SMLM microscopes.

Intracellular structures were easily visualized at super-resolution with our microscope. The LSEC actin cytoskeleton was also easy to visualize, and the resolution of our microscope enabled us to see structures resembling fenestrations, which are encircled by a ring of actin [47]. In a previous study [15] (which used this microscope for actin analysis), NMN and sildenafil were shown to increase the fenestration size, and the actin cytoskeleton is greatly affected by these agents. We report here the full description of the setup and confirm the findings, namely the dramatic condensation of the actin cytoskeleton into stress fibers, and rings of actin became more defined after NMN and sildenafil treatment.

Svistounov et al. [53] proposed that lipid rafts play an integral role in the regulation of fenestration size by pulling or pushing on LSEC sieve plates. We assessed the functionality of the lipid raft stain BodipyGM1 to stain LSECs in the dSTORM context. This stain binds GM1 glycolipids present in lipid rafts, but using single-molecule imaging, we found that it stained all the plasma membrane on LSECs. Some areas of the LSECs stained more intensely with this dye, probably indicative of lipid rafts, but the apparent non-specificity of the stain was initially disappointing. However, further careful analysis of the output revealed that fenestrations were fortuitously also visualized with this lipid raft stain (Figure 5). An explanation for this is that the BodipyGM1 stain, like other commercially available lipid raft stains, is based on the cholera toxin B (CT-B) subunit, which binds GM1 gangliosides. However, a limitation of CT-B is that it binds other cell surface sugars such as galactose [57, 58]. We thus propose that this binding to other cell surface sugars is what we see as background staining (that fortuitously reveals fenestrations), making the BodipyGM1 stain an exciting tool to simultaneously study the relationship between fenestrations and lipid rafts at super-resolution using only one color channel.

We also investigated primary cultures of platelets. Features which particularly captured our interest were super-fine filaments, some thinner than 100 nm, emanating from their plasma membranes. These filaments were membrane structures with an actin skeleton and would be sufficiently long and thin to pass through LSEC fenestrae and, for example, interact with the underlying hepatocytes in the *in vivo* context. Similar interactions of lymphocyte villi with hepatocytes via LSEC fenestrations and vice versa have been shown by Warren et al. [6]. Given that platelets have a role in resolution of fibrosis [8, 9], this super-resolution microscope will be a useful tool to study the platelet: LSEC "synapse" in future studies.

This work thus demonstrates the effectiveness of a custom-built SMLM microscope to perform super-resolution imaging of primary cells for only a small fraction of the cost of a commercial microscope for SMLM. We believe that our work will contribute to the strong current movement of democratizing the access to super-resolution microscopy, making super-resolution available to a wide range of laboratories as a routine lab microscope.

Acknowledgments: The authors are grateful to Marcel Müller for his support with the Micro–Manager-based

camera control. This project was funded by the McKnight Bequest via the Sydney Medical School Foundation and the Ageing and Alzheimers Institute. The publication charges for this article have been funded by a grant from the publication fund of the University of Tromsø – The Arctic University of Norway.

References

[1] Fraser R, Cogger VC, Dobbs B, et al. The liver sieve and atherosclerosis. Pathology 2012;44:181–6.
[2] Sorensen KK, Simon-Santamaria J, McCuskey RS, Smedsrod B. Liver sinusoidal endothelial cells. Compr Physiol 2015;5:1751–74.
[3] McLean AJ, Cogger VC, Chong GC, et al. Age-related pseudocapillarization of the human liver. J Pathol 2003;200:112–7.
[4] Braet F, Wisse E. Structural and functional aspects of liver sinusoidal endothelial cell fenestrae: a review. Comp Hepatol 2002;1:1.
[5] Mohamad M, Mitchell SJ, Wu LE, et al. Ultrastructure of the liver microcirculation influences hepatic and systemic insulin activity and provides a mechanism for age-related insulin resistance. Aging Cell 2016;15:706–15.
[6] Warren A, Le Couteur DG, Fraser R, Bowen DG, McCaughan GW, Bertolino P. T lymphocytes interact with hepatocytes through fenestrations in murine liver sinusoidal endothelial cells. Hepatology 2006;44:1182–90.
[7] Oteiza A, Li R, McCuskey RS, Smedsrod B, Sorensen KK. Effects of oxidized low-density lipoproteins on the hepatic microvasculature. Am J Physiol Gastrointest Liver Physiol 2011;301:G684–93.
[8] Kurokawa T, Ohkohchi N. Platelets in liver disease, cancer and regeneration. World J Gastroenterol 2017;23:3228–39.
[9] Kurokawa T, Zheng YW, Ohkohchi N. Novel functions of platelets in the liver. J Gastroenterol Hepatol 2016;31:745–51.
[10] Grozovsky R, Begonja AJ, Liu K, et al. The Ashwell-Morell receptor regulates hepatic thrombopoietin production via JAK2-STAT3 signaling. Nat Med 2015;21:47–54.
[11] Li Y, Fu J, Ling Y, et al. Sialylation on O-glycans protects platelets from clearance by liver Kupffer cells. Proc Natl Acad Sci USA 2017;114:8360–5.
[12] Bonkowski MS, Sinclair DA. Slowing ageing by design: the rise of NAD(+) and sirtuin-activating compounds. Nat Rev Mol Cell Biol 2016;17:679–90.
[13] Revollo JR, Korner A, Mills KF, et al. Nampt/PBEF/Visfatin regulates insulin secretion in beta cells as a systemic NAD biosynthetic enzyme. Cell Metab 2007;6:363–75.
[14] Boolell M, Allen MJ, Ballard SA, et al. Sildenafil: an orally active type 5 cyclic GMP-specific phosphodiesterase inhibitor for the treatment of penile erectile dysfunction. Int J Impot Res 1996;8:47–52.
[15] Hunt NJ, Lockwood GP, Warren A, et al. Manipulating fenestrations in young and old liver sinusoidal endothelial cells. Am J Physiol Gastrointest Liver Physiol 2019;316:G144–54.
[16] Wisse E. An electron microscopic study of the fenestrated endothelial lining of rat liver sinusoids. J Ultrastruct Res 1970;31:125–50.
[17] Wisse E. An ultrastructural characterization of the endothelial cell in the rat liver sinusoid under normal and various experimental conditions, as a contribution to the distinction between endothelial and Kupffer cells. J Ultrastruct Res 1972;38:528–62.
[18] Wisse E, De Zanger RB, Jacobs R, McCuskey RS. Scanning electron microscope observations on the structure of portal veins, sinusoids and central veins in rat liver. Scan Electron Microsc 1983(Pt 3):1441–52.
[19] Betzig E, Patterson GH, Sougrat R, et al. Imaging intracellular fluorescent proteins at nanometer resolution. Science 2006;313:1642–5.
[20] Hess ST, Girirajan TP, Mason MD. Ultra-high resolution imaging by fluorescence photoactivation localization microscopy. Biophys J 2006;91:4258–72.
[21] Rust MJ, Bates M, Zhuang X. Sub-diffraction-limit imaging by stochastic optical reconstruction microscopy (STORM). Nat Methods 2006;3:793–5.
[22] Ma H, Fu R, Xu J, Liu Y. A simple and cost-effective setup for super-resolution localization microscopy. Sci Rep 2017;7:1542.
[23] Holm T, Klein T, Loschberger A, et al. A blueprint for cost-efficient localization microscopy. Chemphyschem 2014;15:651–4.
[24] Auer A, Schlichthaerle T, Woehrstein JB, et al. Nanometer-scale multiplexed super-resolution imaging with an economic 3D-DNA-PAINT microscope. Chemphyschem 2018;19:3024–34.
[25] Babcock HP. Multiplane and spectrally-resolved single molecule localization microscopy with industrial grade CMOS cameras. Sci Rep 2018;8:1726.
[26] Diekmann R, Till K, Muller M, Simonis M, Schuttpelz M, Huser T. Characterization of an industry-grade CMOS camera well suited for single molecule localization microscopy – high performance super-resolution at low cost. Sci Rep 2017;7:14425.
[27] Van den Eynde R, Sandmeyer A, Vandenberg W, et al. A cost-effective approach to Super-resolution Optical Fluctuation (SOFI) microscopy using an industry-grade CMOS camera. bioRxiv 2018;413179. https://doi.org/10.1101/413179.
[28] Martens KJA, van Beljouw S, van der Els S, et al. An open microscopy framework suited for tracking dCas9 in live bacteria. bioRxiv 2018;437137. https://doi.org/10.1101/437137.
[29] Smedsrod B, Pertoft H. Preparation of pure hepatocytes and reticuloendothelial cells in high yield from a single rat liver by means of Percoll centrifugation and selective adherence. J Leukoc Biol 1985;38:213–30.
[30] Heilemann M, van de Linde S, Schuttpelz M, et al. Subdiffraction-resolution fluorescence imaging with conventional fluorescent probes. Angew Chem Int Ed Engl 2008;47:6172–6.
[31] Hua VM, Abeynaike L, Glaros E, et al. Necrotic platelets provide a procoagulant surface during thrombosis. Blood 2015;126:2852–62.
[32] Nahidiazar L, Agronskaia AV, Broertjes J, van den Broek B, Jalink K. Optimizing imaging conditions for demanding multi-color super resolution localization microscopy. PLoS One 2016;11:e0158884.
[33] Dempsey GT, Vaughan JC, Chen KH, Bates M, Zhuang X. Evaluation of fluorophores for optimal performance in localization-based super-resolution imaging. Nat Methods 2011;8:1027–36.
[34] Edelstein A, Amodaj N, Hoover K, Vale R, Stuurman N. Computer control of microscopes using microManager. Curr Protoc Mol Biol 2010;Chapter 14:Unit14 20.

[35] Tokunaga M, Imamoto N, Sakata-Sogawa K. Highly inclined thin illumination enables clear single-molecule imaging in cells. Nat Methods 2008;5:159–61.
[36] Axelrod D. Cell-substrate contacts illuminated by total internal reflection fluorescence. J Cell Biol 1981;89:141–5.
[37] Arimoto R, Murray JM. A common aberration with water-immersion objective lenses. J Microsc 2004;216(Pt 1):49–51.
[38] Huang F, Hartwich TM, Rivera-Molina FE, et al. Video-rate nanoscopy using sCMOS camera-specific single-molecule localization algorithms. Nat Methods 2013;10:653–8.
[39] Schindelin J, Arganda-Carreras I, Frise E, et al. Fiji: an open-source platform for biological-image analysis. Nat Methods 2012;9:676–82.
[40] Ovesny M, Krizek P, Borkovec J, Svindrych Z, Hagen GM. ThunderSTORM: a comprehensive ImageJ plug-in for PALM and STORM data analysis and super-resolution imaging. Bioinformatics 2014;30:2389–90.
[41] Arganda-Carreras I, Sorzano COS, Marabini R, Carazo JM, Ortiz-De-Solorzano C, Kybic J. Consistent and elastic registration of histological sections using vector-spline regularization. Lect Notes Comput Sci 2006;4241:85–95.
[42] Culley S, Albrecht D, Jacobs C, et al. Quantitative mapping and minimization of super-resolution optical imaging artifacts. Nat Methods 2018;15:263–6.
[43] Wolter S, Loschberger A, Holm T, et al. rapidSTORM: accurate, fast open-source software for localization microscopy. Nat Methods 2012;9:1040–1.
[44] Sommer C, Straehle C, Kothe U, Hamprecht FA. Ilastik: Interactive Learning and Segmentation Toolkit. 2011 8th IEEE International Symposium on Biomedical Imaging: From Nano to Macro. 2011:230–3.
[45] Diekmann R, Helle OI, Oie CI, et al. Chip-based wide field-of-view nanoscopy. Nat Photonics 2017;11:322.
[46] Mönkemöller V, Schuttpelz M, McCourt P, Sorensen K, Smedsrod B, Huser T. Imaging fenestrations in liver sinusoidal endothelial cells by optical localization microscopy. Phys Chem Chem Phys 2014;16:12576–81.
[47] Mönkemöller V, Oie C, Hubner W, Huser T, McCourt P. Multimodal super-resolution optical microscopy visualizes the close connection between membrane and the cytoskeleton in liver sinusoidal endothelial cell fenestrations. Sci Rep 2015;5:16279.
[48] Banterle N, Bui KH, Lemke EA, Beck M. Fourier ring correlation as a resolution criterion for super-resolution microscopy. J Struct Biol 2013;183:363–7.
[49] Legant WR, Shao L, Grimm JB, et al. High-density three-dimensional localization microscopy across large volumes. Nat Methods 2016;13:359–65.
[50] Kiuchi T, Higuchi M, Takamura A, Maruoka M, Watanabe N. Multitarget super-resolution microscopy with high-density labeling by exchangeable probes. Nat Methods 2015;12:743–6.
[51] Sage D, Kirshner H, Pengo T, et al. Quantitative evaluation of software packages for single-molecule localization microscopy. Nat Methods 2015;12:717–24.
[52] Sage D, Pham T-A, Babcock H, et al. Super-resolution fight club: assessment of 2D and 3D single-molecule localization microscopy software. Nat Methods 2019;16:387–95.
[53] Svistounov D, Warren A, McNerney GP, et al. The relationship between fenestrations, sieve plates and rafts in liver sinusoidal endothelial cells. PLoS One 2012;7:e46134.
[54] Bittel AM, Saldivar IS, Dolman NJ, Nan X, Gibbs SL. Superresolution microscopy with novel BODIPY-based fluorophores. PLoS One 2018;13:e0206104.
[55] Bettache N, Baisamy L, Baghdiguian S, Payrastre B, Mangeat P, Bienvenue A. Mechanical constraint imposed on plasma membrane through transverse phospholipid imbalance induces reversible actin polymerization via phosphoinositide 3-kinase activation. J Cell Sci 2003;116(Pt 11):2277–84.
[56] Kwakwa K, Savell A, Davies T, et al. easySTORM: a robust, lower-cost approach to localisation and TIRF microscopy. J Biophotonics 2016;9:948–57.
[57] Munro S. Lipid rafts: elusive or illusive? Cell 2003;115:377–88.
[58] Uesaka Y, Otsuka Y, Lin Z, et al. Simple method of purification of *Escherichia coli* heat-labile enterotoxin and cholera toxin using immobilized galactose. Microb Pathog 1994;16:71–6.

Supplementary Material: The online version of this article offers supplementary material (https://doi.org/10.1515/nanoph-2019-0066).